remote sensing

Article

Characterizing Changes in Geometry and Flow Speeds of Land- and Lake-Terminating Glaciers at the Headwaters of Yarlung Zangbo River, Western Himalayas

Min Zhou [1], Yuzhe Wang [1,*], Tong Zhang [2], Weijun Sun [1] and Yetang Wang [1]

[1] College of Geography and Environment, Shandong Normal University, Jinan 250014, China; 2021010089@stu.sdnu.edu.cn (M.Z.); sunweijun@sdnu.edu.cn (W.S.); yetangwang@sdnu.edu.cn (Y.W.)
[2] State Key Laboratory of Earth Surface Processes and Resource Ecology, Beijing Normal University, Beijing 100875, China; tzhang@bnu.edu.cn
* Correspondence: wangyuzhe@sdnu.edu.cn

Abstract: The glaciers of the Himalayas are essential for water resources in South Asia and the Qinghai–Tibet Plateau, but they are undergoing accelerated mass loss, posing risks to water security and increasing glacial hazards. This study examines long-term changes in the geometry and flow speeds of both land- and lake-terminating glaciers at the headwaters of the Yarlung Zangbo River, using field measurements, remote sensing, and numerical ice flow modeling. We observed significant heterogeneity in glacier behaviors across the region, with notable differences between glacier terminus types and even among neighboring glaciers of the same type. Between 1974 and 2020, glacier thinning and mass loss rates doubled in the early 21st century (-0.57 ± 0.05 m w.e. a^{-1}) compared to 1974–2000 (-0.24 ± 0.11 m w.e. a^{-1}). While lake-terminating glaciers generally experienced more rapid retreat and mass loss, the land-terminating N241 Glacier displayed comparable mass loss rates. Lake-terminating glaciers retreated by over 1000 m between 1990 and 2019, while land-terminating glaciers retreated by less than 750 m. The ITS_LIVE velocity dataset showed higher and more variable flow speeds in lake-terminating glaciers. Numerical modeling from 2000 to 2017 revealed divergent changes in flow regimes, with lake-terminating glaciers generally experiencing acceleration, while land-terminating glaciers showed either a slowing down or stable flow behavior. Our findings underscore the significant role of lake-terminating glaciers in contributing to ice mass loss, emphasizing the need for advanced glacier models that incorporate dynamic processes such as frontal calving and longitudinal coupling.

Keywords: glacier mass change; lake-terminating glacier; flow regime modeling; Yarlung Zangbo River; Himalaya

Academic Editor: Xianwei Wang

Received: 14 October 2024
Revised: 22 December 2024
Accepted: 23 December 2024
Published: 26 December 2024

Citation: Zhou, M.; Wang, Y.; Zhang, T.; Sun, W.; Wang, Y. Characterizing Changes in Geometry and Flow Speeds of Land- and Lake-Terminating Glaciers at the Headwaters of Yarlung Zangbo River, Western Himalayas. *Remote Sens.* **2025**, *17*, 40. https://doi.org/10.3390/rs17010040

1. Introduction

The Himalayas, spanning over 2400 km from west to east, are profoundly influenced by the Indian monsoon and the mid-latitude westerlies [1]. This region stands as the most heavily glacierized area in the low latitudes of the Earth, harboring the largest ice volume outside the polar regions [2]. Himalayan glaciers serve as vital water resources for densely populated regions in South Asia and the Qinghai–Tibet Plateau [3,4], playing a critical role in downstream river runoff and modulating seasonal variability [5–7]. Furthermore, meltwater from these glaciers sustains essential ecosystem services that are crucial for socio-economic development in mountainous areas, including agricultural irrigation, hydropower generation, and domestic water supply [8–10].

Himalayan glaciers have been experiencing mass loss over several decades [11,12], with a twofold increase in loss rates observed since the 21st century [13–15]. This trend poses challenges to regional water security and increases risks of glacial hazards (e.g., glacial lake outburst floods and ice avalanches) [16,17]. Due to diverse climate patterns, the glacier mass loss rates across the Himalayas exhibit high spatial heterogeneity [18,19]. However, large variations in mass balances among individual glaciers within the region were also documented [13,20,21], suggesting that there are factors partly independent of climate that affect the processes of mass changes. One important factor is the rapid growth of proglacial lakes during recent decades in the Himalayas [22–26]. The proglacial lake expansion can affect the glacier ablation through frontal calving and subaqueous melt [23,26], and it can also influence the longitudinal coupling stress and basal slip, thereby impacting ice dynamics and mass balance [27,28]. Remote-sensing studies have revealed the contrasting patterns of mass and velocity changes between lake- and land-terminating glaciers in the Himalayas [29–31]. Generally, the lake-terminating glaciers lose more mass and flow faster than land-terminating glaciers [23,30,31]. Proglacial lakes elevate subglacial water pressure, reducing effective pressure and enhancing basal sliding, which accelerates glacier motion. Additionally, the presence of a proglacial lake alters the longitudinal stress balance, decreasing resistive stresses at the terminus and promoting faster ice flow upstream. As a result, the ice-contact lakes complicate glacier mass balance and dynamics, posing modeling challenges for future glacier projection [32]. It is therefore crucial to investigate the multi-decadal changes in both the mass and velocity of Himalayan glaciers, which would provide further insights into their nonlinear response to climate change and lake evolution.

Previous studies have revealed statistically robust differences in surface elevation and velocity changes between lake- and land-terminating glaciers [24,25,29–31]. However, the majority of these investigations have been concentrated in the eastern Himalaya. A recent investigation by Scoffield et al. suggests that these differences are insignificant in the western Himalayas due to earlier evolutionary stages of ice-contact lakes in this area compared to those in the eastern Himalaya [33]. Nonetheless, the number of ice-contact lakes in the western Himalayas is projected to substantially increase by 2100, indicating that future ice loss may become pronounced due to lake expansion [34]. Observations of glacier changes in the western Himalayas can help us to understand their dynamic behaviors, especially those of lake-terminating glaciers at the early development stage. Elucidating the key processes in glacier-lake interactions will be crucial for developing process-based glacier dynamics models and improving large-scale glacier projections.

Space-based measurements have been extensively used to monitor Himalayan glacier changes at various geographic scales. However, the accuracy of these satellite-derived results is often limited by the lack of field data. Due to logistical challenges, field measurements in the Himalayas are restricted to only a few glaciers [35], and are particularly scarce on lake-terminating glaciers [30], thereby constraining the calibration and validation processes. While numerical glacier evolution models have been utilized to project future glacier changes [36–38], few of these models explicitly incorporate the dynamics of lake-terminating glaciers. Consequently, they are unable to fully capture the impacts of proglacial lakes on glacier evolution. Numerical ice flow modeling is of importance for understanding the physical mechanisms underlying lake-terminating glacier changes and provides valuable insights into stress balance and flow regime changes. Current studies often employ simplified analysis using shallow-ice approximation models [31]. However, a more sophisticated model, such as a higher-order model, is essential for comprehensively understanding the flow regimes of glaciers with different terminus types.

This study investigates the long-term changes in land- and lake-terminating glaciers at the headwaters of the Yarlung Zangbo River (YZR) in the western Himalayas. Our aims are to reveal the temporal impacts of proglacial lakes on glacier mass and velocity changes and to contrast the distinct dynamic behaviors of these two types of glaciers within the same region. To achieve this, we use multi-source digital elevation models (DEMs) to calculate multi-decadal changes in glacier surface elevation. We validate the satellite-derived High Mountain Asia (HMA) glacier velocity product using field measurements from our study region. We then assess glacier surface velocity changes using this satellite-derived product. Additionally, we track the terminus changes of representative glaciers to examine the interaction between glaciers and lakes, thereby enhancing our understanding of glacier mass and velocity changes. We select geodetic mass balance, surface velocity, and terminus change to compare the behaviors of land- and lake-terminating glaciers, as these parameters capture key aspects of glacier response to both climatic and lake-induced factors. Finally, we employ a higher-order ice flow model to investigate changes in glacier flow speed regimes by assimilating satellite-derived velocities.

2. Study Area

Our study area is located on the northern slope of the Himalayas and serves as the headwaters of the YZR. The study area is defined based on the geographical extent of topographical maps (see Section 3.2), spanning ∼30°0′–30°25′N and ∼82°0′–82°40′E (Figure 1). The average altitude of this area exceeds 5000 meters a.s.l., and the climate is semi-arid with dry and cold characteristics. This aridity is due to the Himalayas blocking moisture from the Indian monsoon and the Karakoram range blocking moisture from the westerlies.

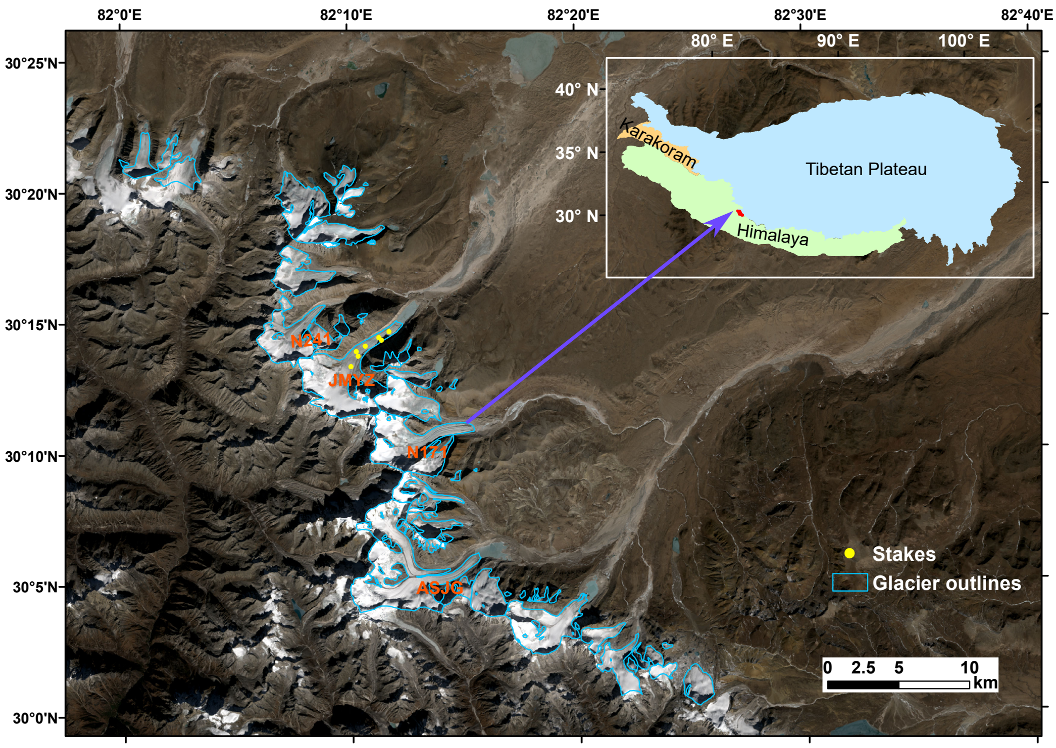

Figure 1. Overview of the study area. Glacier outlines from the CGI2 are shown in blue. Stakes are marked with yellow circles, and representative glaciers are labeled in red. The background image is a Landsat 8 scene. The inset map indicates the location of the study area within the HMA region.

There are 25 glaciers in this region with areas larger than 1 km^2. These glaciers are classified as subcontinental type and flow northwards onto the southwestern Tibetan

Plateau. According to the second Chinese glacier inventory (CGI2), almost all glaciers in this region are debris-free and primarily land-terminating. However, a few glaciers terminate in proglacial lakes, making them lake-terminating (Figure 1). This region, therefore, provides an ideal setting to compare the changes between land-terminating and lake-terminating glaciers.

For a detailed analysis of changes in the mass, velocity, and flow regimes, we selected four glaciers based on specific criteria. Two are lake-terminating glaciers: Jiemayangzong (JMYZ) Glacier and Asejiaguo (ASJG) Glacier. These glaciers are definitively identified as lake-terminating in the study region and are relatively large, which helps to reduce uncertainties associated with coarse remote-sensing datasets. Additionally, surface velocity measurements from JMYZ Glacier provide valuable validation data for our analysis. To compare lake-terminating glaciers with land-terminating ones, we selected two nearby land-terminating glaciers (GLIMS IDs: G082213E30171N and G082128E30241N), referred to as N171 and N241. These glaciers were chosen based on their proximity to the lake-terminating glaciers, ensuring similar environmental conditions and comparable sizes, allowing for a meaningful comparison of dynamic behavior.

3. Data and Methods

3.1. Glacier Outlines and Types

We used the glacier outlines from the CGI2, which was derived from the Landsat images [39]. The glaciers in our study region were classified as either land-terminating or lake-terminating types. We identified the lake-terminating glaciers by combining data from CGI2 and the HMA glacial lake inventory [40], the latter of which provides glacial lake boundaries for 1990 and 2018. Glaciers were classified as lake-terminating if contact between the terminus and a proglacial lake was evident in both 1990 and 2018. The identified lake-terminating glaciers were further verified through manual interpretation of Landsat images obtained in 1990 and 2018 to ensure that the glaciers terminated into the lakes. Based on the CGI2 glacier outlines, we manually digitalized the glacier terminus between 1990 and 2019 with a time interval of approximately 5 years.

3.2. Digital Elevation Models

In this study, we used multiple DEMs to assess glacier surface elevation changes, including TOPO DEM and SRTM DEM. Six TOPO DEMs were digitized from 1:50,000 scale topographic maps produced by the Chinese Military Geodetic Service in October 1974, based on aerial stereo pairs. Contours and elevation points from these maps were used to construct a triangulated irregular network, which was then used to generate the TOPO DEMs. The spatial reference systems of the maps were transformed from the Beijing Geodetic Coordinate System 1954 and Yellow Sea 1956 datum to the World Geodetic System 1984 (WGS84) and Earth Gravity Model 1996 (EGM96) using a seven-parameter transformation method. The vertical accuracy of the TOPO DEMs was estimated to be $\pm$8 m [41].

The SRTM DEM, derived from C-band radar images with an original resolution of 3 arc seconds (approximately 90 m), was collected by NASA in February 2000. Due to its continuous spatial coverage, the C-band DEM was selected for this study. The SRTM DEM has been widely used in geodetic glacier mass balance estimation [42–44]. Its horizontal and vertical datums are WGS84 and EGM96, respectively.

We also used the TanDEM-X DEM, a global product with a 90 m spatial resolution, to obtain glacier surface elevations. The TanDEM-X mission aimed to generate accurate 3D land surface models using Synthetic Aperture Radar (SAR) technology aboard the TanDEM-X and TerraSAR-X satellites. DEM data for this region were obtained from multiple radar images taken around 2017. The absolute horizontal and vertical errors of the TanDEM-X DEM were both less than 10 m [45]. The WGS84 ellipsoid heights of the TanDEM-X DEM were converted to EGM96 geoid heights using the MATLAB 2016b

3.3. Glacier Mass Changes

In this study, we calculated glacier mass changes for the period 1974–2000 by differentiating the TOPO and SRTM DEMs. To extend these results to the past two decades, we incorporated an open-access global glacier elevation change product derived from the time series of DEMs with a spatial resolution of 100 m [46]. We refer to this as the Hugonnet dataset. For our analysis, we utilized the elevation change maps from the Hugonnet dataset for the periods 2000–2010, 2010–2020, and 2000–2020. The methods used for calculating glacier mass changes and the associated uncertainty assessment are described below.

Co-registration of DEMs is a prerequisite before performing the differencing. First, both DEMs were resampled to a 90 m spatial resolution and reprojected to the same projection system (WGS84, UTM 44N). We co-registered the TOPO DEM to the SRTM DEM over stable terrain following the Nuth and Kääb method [47]. Stable terrain pixels were selected outside the glaciers with slopes between 5° and 45°. This method iteratively computes the shift vector by relating elevation differences to terrain slope and aspect.

The SRTM DEM, derived from C-band radar images, can be biased due to radar wave penetration into ice and dry snow [48]. To correct this bias, we applied a linear model that estimates radar penetration depth (d_p) based on altitude (z) [49]. This model assumes a linear relationship between altitude and radar penetration depth across a $1^\circ \times 1^\circ$ grid in HMA. For our study area, the local relationship $d_p = 0.00355z - 18.2$ was used. The average penetration depth in this region was estimated to be around 2.0 m.

After performing DEM differencing, we removed outliers where the elevation change (Δh) exceeded 100 m or the slope was steeper than 45°. Additionally, we filtered out pixels with elevation differences outside the 31.7% to 68.3% quantile range, following the approach recommended by [50]. Finally, we converted glacier elevation changes to mass changes (ΔM) using the following equation:

$$\Delta M = \rho_c A_g \Delta h \tag{1}$$

where $\rho_c = 850$ kg m^{-3} is the density conversion factor from volume to mass [51] and A_g is the glacier area.

We calculated the uncertainties in mass change by considering four main sources of error: uncertainty in elevation change ($\sigma_{\Delta h}$), uncertainty in glacier area (σ_{A_g}), uncertainty in the density conversion factor (σ_{ρ_c}), and uncertainty in the C-band penetration depth (σ_{d_p}). Assuming that these four error components are independent, the total uncertainty in mass change, $\sigma_{\Delta M}$, is given by

$$\sigma_{\Delta M} = |\Delta M| \sqrt{\left(\frac{\sigma_{\Delta h}}{\Delta h}\right)^2 + \left(\frac{\sigma_{A_g}}{A_g}\right)^2 + \left(\frac{\sigma_{\rho_c}}{\rho_c}\right)^2 + \left(\frac{\sigma_{d_p}}{\Delta h}\right)^2}. \tag{2}$$

We quantified $\sigma_{\Delta h}$ using the normalized median absolute deviation (NMAD) of the elevation change estimates over stable terrain [52], which is given by

$$\sigma_{\Delta h} = \frac{\sigma_p}{\sqrt{N_{\text{eff}}}}, \tag{3}$$

where σ_p is the NMAD of the elevation changes on stable terrain, and N_{eff} is the effective number of independent values on stable terrain, calculated as

$$N_{\text{eff}} = \frac{N_{\text{tot}} \cdot P_s}{2 \cdot l}, \tag{4}$$

where N_{tot} is the total number of values, P_s is the pixel size of the DEM differencing image, and l is the spatial autocorrelation distance (500 m). The area uncertainty, σ_{A_g}, is assumed to be 8% of the glacier area [53]. The uncertainty in the density conversion factor, σ_{ρ_c}, is $\pm$60 kg m^{-3} [51]. The penetration depth uncertainty, σ_{d_p}, is estimated for our glacierized region (elevation range 4700–6500 m), accounting for the slope error ($\pm 2.7 \times 10^{-4}$) and intercept error ($\pm$1.301 m) from the linear relationship.

3.4. Glacier Surface Velocities

We used ITS_LIVE (Inter-Mission Time Series of Land Ice Velocity and Elevation) product to examine the spatio-temporal changes in glacier surface velocity. The ITS_LIVE data product used here is a set of compilations of annual mean surface velocities for HMA. It was derived from Landsat 4, 5, 7, and 8 imagery using a feature-tracking algorithm through the auto-RIFT pipeline [54]. It spans the time period from 1985 to 2018 with a spatial resolution of 240 m. We extracted the average surface velocities along the glacier centerlines using bilinear interpolation method between 1985 and 2018.

Although ITS_LIVE glacier velocity product has been widely used in glaciological studies [55,56], its accuracy remains unclear, particularly in the Himalayas. Here we used in situ surface horizontal velocity measurements on the JMYZ Glacier to assess the applicability of ITS_LIVE in our study region. Repeated stake measurements were carried out on 1 October 2010 and 26 May 2011 using differential global positioning system (Figure 1). Due to logistical difficulty and remoteness, only seven stakes were installed in the ablation zone, and the measurements did not cover a complete hydrological year, with a data gap in summer. Satellite-derived seasonal glacier velocity in the western Himalayas suggested that the peak flow speed occurred in spring, which was much larger than the summer speed [57,58]. To derive the annual average glacier velocities from stake measurements, we thus multiplied the measured velocities by a constant factor of 0.7, following [57,58].

Before we quantify the glacier velocity changes using ITS_LIVE product in our study region, we first evaluate its performance in comparison to measured surface velocities on the JMYZ Glacier. As the time span of stake measurements overlaps the acquisition dates of annual ITS_LIVE velocities in 2010, 2011, and 2012, we extract the ITS_LIVE velocities at the stakes and along the centerline in these three years using a bilinear interpolation method. Figure 2 compares the mean annual ITS_LIVE velocities between 2010 and 2012 with our measurements. It shows that the ITS_LIVE velocities are in good agreement with the measurements except, at stakes A and B (Figure 2a). The mean absolute deviation between ITS_LIVE and measured velocities is 7.2 m a^{-1}, corresponding to 25% of the largest measured velocities. However, the mean absolute deviation significantly decreases to 2.7 m a^{-1} (corresponding to 10% of the largest measured velocities) after excluding the data at stakes A and B. The mismatch at these stakes is possibly due to the coarse resolution of ITS_LIVE or localized failures in feature tracking. Additionally, the placement of the stakes, which were approximately along the glacier centerline, may have contributed to the observed discrepancies (Figure 1). Figure 2b shows that the ITS_LIVE velocities generally capture the spatial pattern of surface flow speed changes on the JMYZ Glacier. Through our comparisons, we think that ITS_LIVE product is relatively reliable and can be applied to our study.

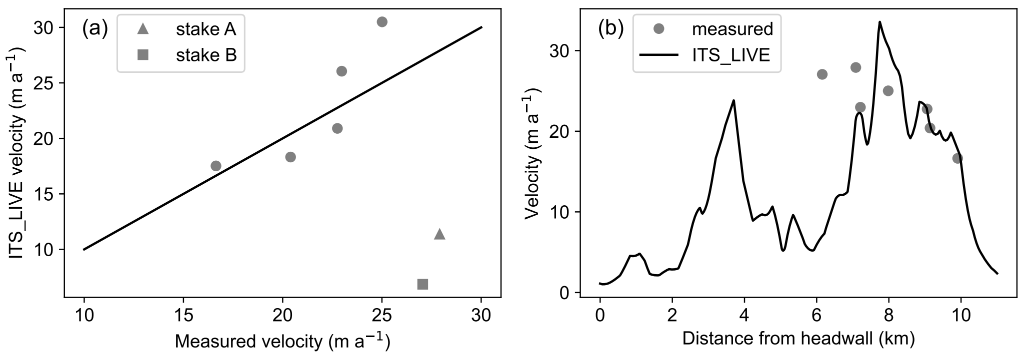

Figure 2. Comparison between ITS_LIVE velocities and measured velocities at the stakes (**a**) and along the glacier centerline (**b**). Stakes A and B are indicated by triangle and square.

3.5. Glacier Thicknesses

We used the ice thickness data as an input for am ice flow model to simulate the glacier flow regimes. The ice thickness data utilized in this study were derived from the composite product developed by [59], which provides a consensus estimate of the ice thickness distribution for global glaciers. This dataset was generated through a combination of up to five different models utilizing principles of ice flow dynamics to invert for ice thickness from surface characteristics, such as elevation and slope. The models were assessed for performance against field-measured ice thicknesses through a cross-validation scheme, and the final composite solution is obtained by applying inverse variance and bias weighting to the individual model outputs. This ice thickness dataset enhances our understanding of glacier volume and provides critical inputs for numerical ice flow models.

3.6. Glacier Flow Regime Modeling

We used the numerical ice flow model PoLIM to infer the flow regimes of four typical glaciers in our study region (see Section 2) for two different years, approximately 2000 and 2017, by assimilating the ITS_LIVE velocity dataset. By comparing these two flow regimes, we investigated the impacts of lake evolution and surface elevation changes on glacier dynamics. PoLIM is a Blatter–Pattyn-type higher-order flowband model with the inclusion of longitudinal stress [60], which is essential for accurately modeling mountain glacier dynamics. For simplicity, we describe only the boundary conditions of the PoLIM model to aid our understanding of the inversion process, with detailed physical descriptions provided in [60].

At the glacier surface, a stress-free surface boundary condition is assumed. For PoLIM, this boundary condition reads

$$(2\tau_{xx} + \tau_{yy})\frac{\partial s}{\partial x} - \tau_{xz} = 0. \tag{5}$$

At the glacier bedrock, a linear friction law is applied, which relates the basal drag τ_b to the sliding velocity u_b:

$$\tau_b = -\beta^2 u_b, \tag{6}$$

where β^2 is the basal friction parameter and is positive.

Longitudinal glacier topographies, including ice thickness, surface, and bed elevations, are necessary inputs for the PoLIM model. We first extracted the surface elevation from the SRTM DEM (referred to as s_{srtm}) and the ice thickness (referred to as H_{2000}) along the centerline. The bedrock elevation b was then derived by substracting the ice thickness H_{2000} from the SRTM elevation s_{srtm}. Assuming a fixed bedrock topography, we calculated the ice thickness in 2017 (H_{2017}) using the equation $H_{2017} = s_{\text{tandem}} - b$, where s_{tandem} represents the TanDEM-X DEM elevation. It is worth noting that we consider the year used here to be the calendar year.

We utilized the Robin inversion method implemented in PoLIM to infer glacier flow regimes [61]. This method is a numerical approach developed to solve the inverse problem of determining optimal basal conditions from glacier topography and surface velocity observations [62–64]. It iteratively solves the higher-order approximated equations with two types of boundary conditions, i.e., a Neumann condition (see Equation (5)) and a Dirichlet condition representing the free surface and measured velocities, respectively. The method uses a cost function to minimize the mismatch between modeled and observed velocities, and iteratively adjusts the basal friction parameter β^2 to achieve this minimization. The Dirichlet condition at the surface is set as

$$u(s) = u_{\text{itslive}}, \tag{7}$$

where $u(s)$ is the horizontal surface velocity and u_{itslive} is the ITS_LIVE velocitity. To reduce the uncertainty inherent in ITS_LIVE, we adopted the mean velocities from the periods 1999–2001 and 2016–2018 as representative values for the years 2000 and 2017, respectively. For simplicity, we negeleted the thermo-mechanical coupling effect and assumed a constant flow rate factor A. Through assimilating ITS_LIVE velocities and adjusting the basal friction parameters, we therefore modeled the horizontal velocity fields using the given glacier topographies.

4. Results

4.1. Geodetic Glacier Mass Balance Changes

Almost all glaciers experienced thinning during 1974–2000, with ice loss rates significantly intensifying in the first two decades of the 21st century, particularly at the glacier tongues (Figure 3a,b). The average regional geodetic mass balances for these periods were -0.24 ± 0.11 m w.e. a^{-1} and -0.57 ± 0.05 m w.e. a^{-1}, respectively, indicating a twofold increase in the ice loss rate. Figure 3c illustrates the region-wide average mass balance profile versus elevation. Notably, the 2000–2020 geodetic mass balance profile was considerably steeper compared to that of 1974–2000. The differences in ice loss rates between the two intervals markedly increased with decreasing elevation, peaking at nearly 2.0 ± 0.05 m w.e. a^{-1} below an elevation of 5000 m. We observe that the loss rates in the 1974–2000 profile were relatively steady across elevations of 5600–6000 m, with small fluctuations around the mean value of -0.16 ± 0.05 m w.e. a^{-1}. Below an elevation of 5600 m, the loss rates increased significantly, while, in the 2000–2020 profile, the loss rates sharply decreased below an elevation of 6250 m.

Figure 4 shows the temporal variations in geodetic mass balances along the centerlines of four selected glaciers over the periods 1974–2000, 2000–2010, and 2010–2020. We found that the geodetic mass balances of the four glaciers at lower elevations have become significantly more negative since the start of the 21st century. However, the signals of temporal variations in ice thickness changes at the upper areas of individual glaciers were relatively noisy, particularly for the profiles derived from the Hugonnet dataset. These profiles displayed jagged oscillations in geodetic mass balances, which changed rapidly over short spatial distances. For example, the 2000–2010 geodetic mass balance of the JMYZ Glacier showed sharp fluctuations at distances of approximately 1.5 to 4.0 km from the glacier headwall, reaching a peak of 4.4 ± 0.05 m w.e. a^{-1} at around 1.6 km, before dropping to a minimum of -7.8 ± 0.05 m w.e. a^{-1} at approximately 3.2 km. This phenomenon was likely caused by uncertainties in DEM production, resulting from low radiometric contrast in areas at high elevations covered by snow and firn. Therefore, we focus our analysis on the mid- and low-elevation areas.

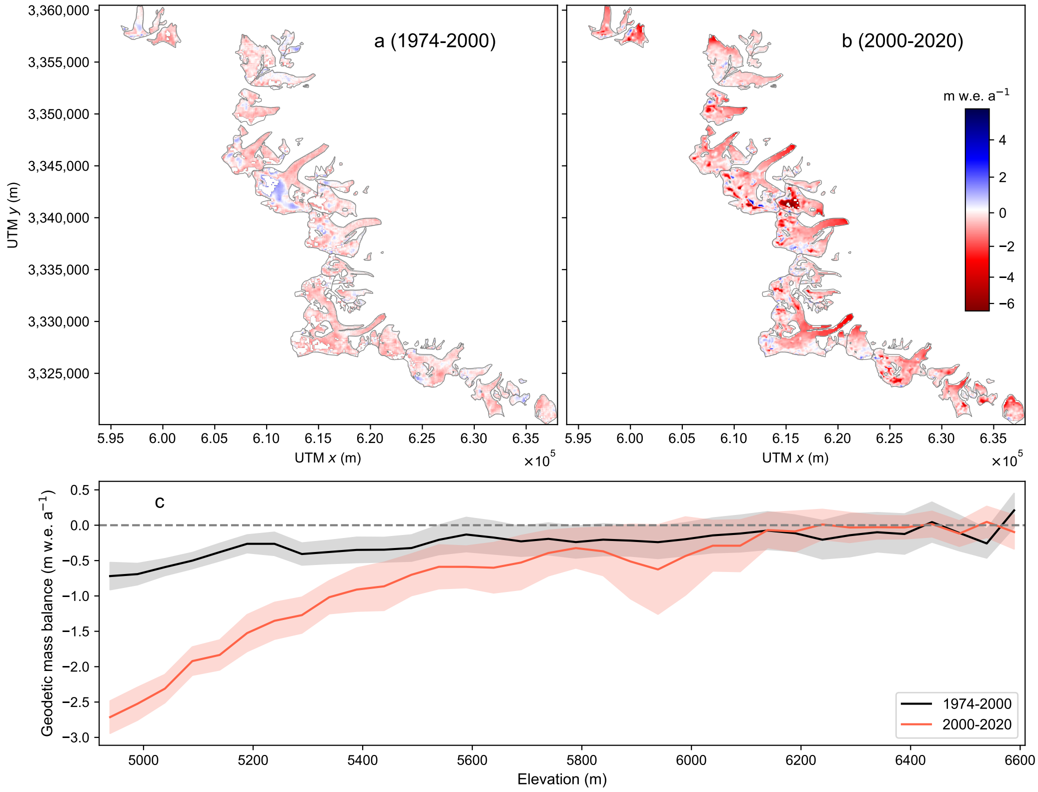

Figure 3. Comparison of region geodetic mass balances between 1974–2000 and 2000–2020. (**a**) Regional geodetic mass balances for individual glaciers during the period 1974–2000. (**b**) Regional geodetic mass balances for individual glaciers during the period 2000–2020. Note that panels (**a**,**b**) share the same colorbar scale. (**c**) Altitudinal distributions of geodetic mass balances separated into 50 m elevation bins during the two intervals. Shaded areas indicate the standard error of the mean.

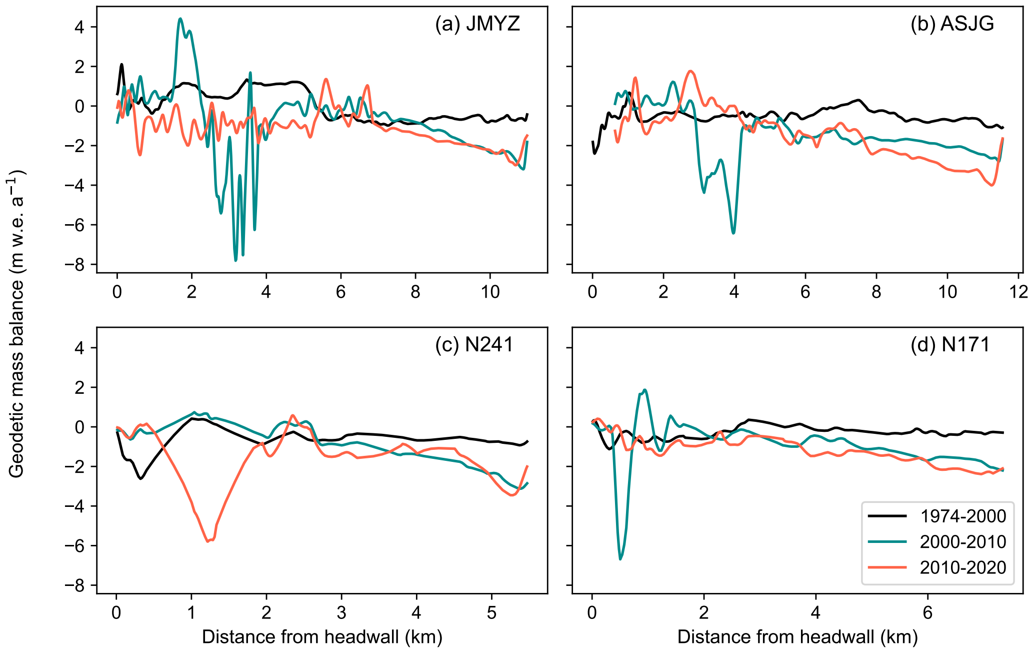

Figure 4. Comparison of geodetic mass balances along the centerlines of four glaciers for the periods 1974–2000 (black), 2000–2010 (cyan), and 2010–2020 (red). (**a**) JMYZ Glacier. (**b**) ASJG Glacier. (**c**) N241 Glacier. (**d**) N171 Glacier.

The mass balance profiles at the tongues of lake-terminating glaciers (Figure 4c,d) were notably less smooth compared to those of land-terminating glaciers (Figure 4a,b), highlighting the influence of proglacial lakes on ice thickness changes. In general, lake-terminating glaciers showed greater ice loss at their termini than land-terminating glaciers. However, N241 Glacier exhibited a similar pattern of accelerated ice thinning as seen in the lake-terminating glaciers (Figure 4c), suggesting that land-terminating glaciers can also experience comparable rates of ice loss. The most significant ice reduction for the JMYZ Glacier occurred during the 2000–2010 period, while the ASJG Glacier's greatest ice loss rate was recorded during 2010–2020. This suggests that the mass loss of lake-terminating glaciers may be linked to the evolutionary stages of proglacial lakes. Although the land-terminating N171 Glacier experienced intensified ice loss from 1974–2000 to 2010–2020, its geodetic mass balance decreased steadily toward the terminus (Figure 4d).

The sudden change in geodetic mass balance (2010–2020) observed at the termini of the JMYZ, ASJG, and N241 Glaciers is primarily due to glacier retreat over time (Figure 4a–c). As the centerline extends into areas that have become ice-free , the elevation change in these regions is minimal, leading to mass balance values approaching zero. This effect is most pronounced for the 2010–2020 period. For the N171 Glacier, however, the smaller terminus retreat resulted in little to no change (Figure 4d).

4.2. Glacier Velocity Changes

We investigated the spatio-temporal glacier speed changes in our study region using the time series of ITS_LIVE velocities for the period of 1990–2018. Figure 5 shows the multi-year averaged velocity maps for the periods 1990–1999, 2000–2009, and 2010–2018. Here, we used the 2010–2018 velocity map to demonstrate the regional flow speed characteristics (Figure 5c). We can see that large glaciers generally flowed faster than small glaciers. The highest flow speed was more than 40 m a^{-1} occurring at the JMYZ Glacier. The glacier-wide mean velocity across this region ranged from 0.4 m a^{-1} to 11.1 m a^{-1}. Lake-terminating glaciers exhibit substantially higher surface velocities and larger areas compared to land-terminating glaciers. From 2000–2018, ASJG and JMYZ had glacier-wide mean velocities of 10.0 m a^{-1} and 8.5 m a^{-1}, respectively, while land-terminating glaciers averaged 2.3 m a^{-1}. Together, ASJG and JMYZ comprise 27.5% of the total glacierized area in the region, highlighting the distinct dynamic and geometric characteristics of these two glacier types.

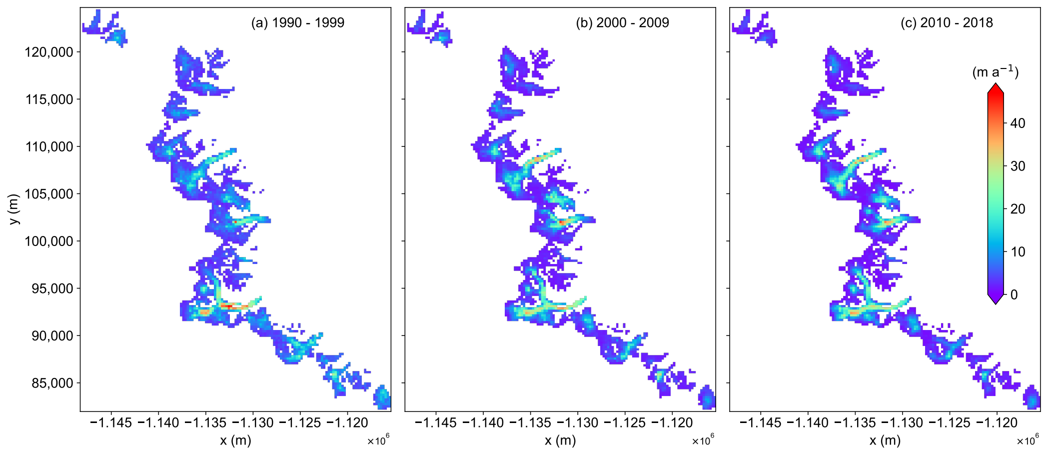

Figure 5. Region-wide glacier velocity maps for the periods 1990–1999 (**a**), 2000–2009 (**b**), and 2010–2018 (**c**).

To characterize the regional velocity trends, we examined the temporal velocity changes for the four selected glaciers along the centerlines (Figure 6). We can see that the spatial patterns of lake-terminating glacier velocity profiles were more complex than those of land-terminating glaciers, which generally showed a single maximum velocity pattern. Although the selected glaciers were exposed to similar environmental settings, their temporal velocity trends were significantly different. The surface velocities of the JMYZ Glacier were at a relatively low level, less than 23 m a^{-1}, in the 1990s (Figure 6a). In 2000s, however, the surface velocities substantially increased, particularly at the glacier terminus (6.0–11.0 km). The maximum velocity increased by 54% and reached 34.7 m a^{-1}. During the period 2010–2018, the terminus velocity decreased slightly, but the velocity in the upper profile (2.2–7.7 km) showed a pronounced increase. For the ASJG Glacier, its velocity trends during the investigated period were more complicated than the JMYZ Glacier (Figure 6b). It exhibited a high flow regime in the 1990s, with a mean value of 17.2 m a^{-1} and a maximum value of 38.4 m a^{-1}. In the 2000s, we observed a significant velocity slowdown along most sections of the profile. Velocity increase only occurred in the upper section (2.1–3.1 km) and at the glacier tongue (10.5–11.5 km). The surface velocities during the period 2010–2018 showed further slowdown, particularly at the glacier front. For the land-terminating glaciers, i.e., N241 Glacier and N171 Glacier, they exhibited relatively simple patterns of longitudinal velocities compared to lake-terminating glaciers (Figure 6c,d). The N241 Glacier showed a significant speedup since the 2000s (Figure 6c). The maximum velocity increased by about 60% from 12.6 m a^{-1} in the 1990s to 20.1 m a^{-1} for the period 2010–2018. However, the terminus velocities showed a gradual slowdown over the investigated period. For the N171 Glacier, its mean surface velocity was approximately two times higher than the N241 Glacier. It also showed speedup since the 2000s, particularly in the central section. During the period 2010–2018, a slight speed increase was observed in the upper section (0.5–3.7 km), but the peak velocity decreased. The terminus velocity of the N171 Glacier also exhibited gradual reductions since the 1990s.

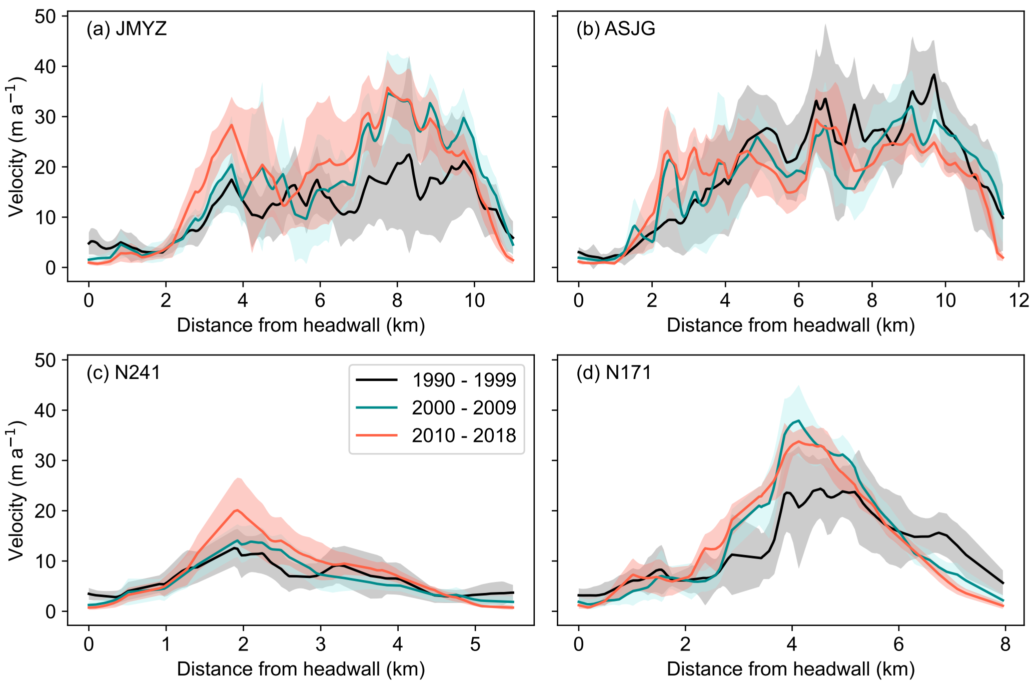

Figure 6. Comparison of surface velocities along the centerlines of four glaciers for the periods 1990–1999 (black), 2000–2009 (cyan), and 2010–2018 (red). (**a**) JMYZ Glacier. (**b**) ASJG Glacier. (**c**) N241 Glacier. (**d**) N171 Glacier. The shaded areas indicate the standard deviations.

4.3. Glacier Terminus Changes

Figure 7 shows the terminus positions of the four glaciers between 1990 and 2019 with a temporal resolution of approximately five years. It is evident that all glaciers have significantly retreated over the past three decades. The recession of lake-terminating glaciers (JMYZ and ASJG) was larger in both magnitude and rate compared to land-terminating glaciers (N241 and N171). Specifically, the lake-terminating glaciers retreated more than 1000 m during the study period 1990–2019, while the land-terminating glaciers retreated less than 750 m. Among them, the length change of land-terminating glacier N171 was the smallest, approximately −516 m over the study period. In contrast, the ASJG Glacier had the most significant length change, approximately −1600 m, which was three times the length change of the N171 Glacier. The ASJG Glacier also exhibited the fastest retreat rate compared to the other three glaciers in all epochs between 1990 and 2019. The retreat rates of the glacier termini showed no clear overall trend during the study period. However, the maximum retreat rates for all glaciers occurred between 2005 and 2010, with the ASJG Glacier receding at a rate of more than 70 m a^{-1}. During the period 2015–2019, the lengths of all glaciers significantly reduced, and the retreat rate of the land-terminating glacier N241 (40.5 m a^{-1}) was comparable to that of the lake-terminating JMYZ Glacier (39.4 m a^{-1}).

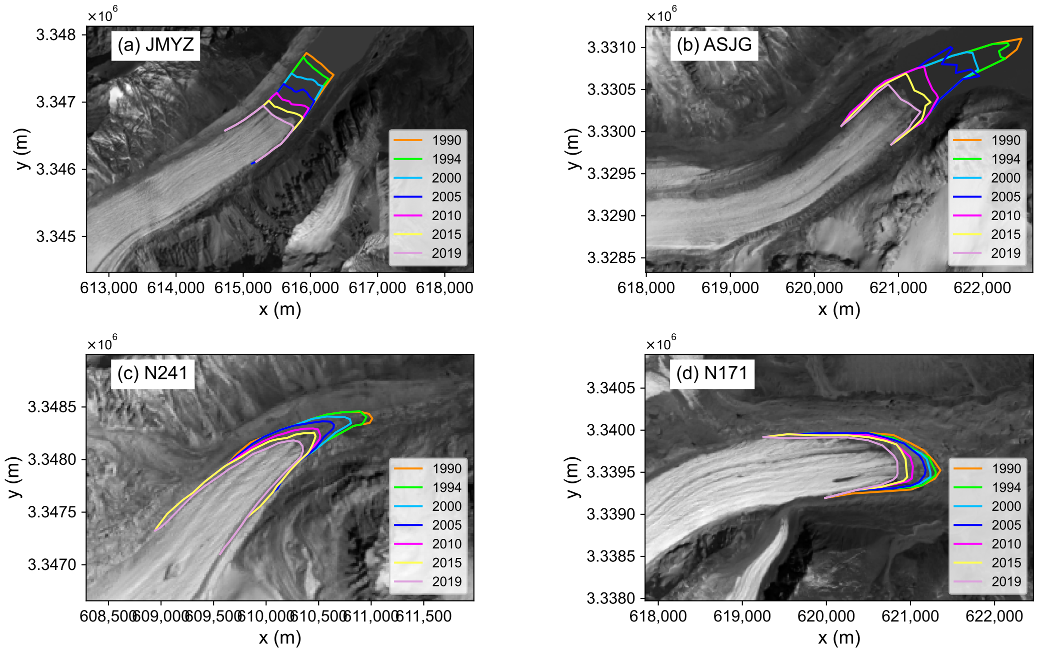

Figure 7. Temporal changes in glacier termini from 1990 to 2019 for four glaciers. (**a**) JMYZ Glacier, (**b**) ASJG Glacier, (**c**) N241 Glacier, (**d**) N171 Glacier. The background in each panel is a Landsat 8 image.

4.4. Modeled Glacier Flow Regimes

Figures 8 and 9 show the modeled horizontal velocity fields in 2000 and 2017 along the longitudinal profiles for the lake- and land-terminating glaciers, respectively. Unlike the surface velocity profiles shown in Figure 6, the velocity fields are capable of capturing changes in interior and basal flow speeds responding to variations in glacier geometry, bed condition, and proglacial lake. To help understanding the flow regime changes, the modeled surface and basal velocities through robin inversion were also presented (Figure 10).

We observed that the selected glaciers display distinct flow regimes regardless of their terminus types. For the lake-terminating glaciers, the changes in their flow patterns showed significant differences. The flow regime of JMYZ displayed a clear speedup between 2000 and 2017 (Figure 8a,c). The high flow speed zone migrated upstream from the terminus towards the headwall during the study period. The increased flow speeds occurred not only on the glacier surface as shown in Figure 10a but also within its interior (Figure 8c). For the other lake-terminating glacier ASJG, its flow velocity field generally decreased with substantial surface thinning (Figure 8b,d). In 2000, the highest velocity zone was located at the glacier terminus. However, by 2017, the terminus speeds significantly decreased, and the high-flow zone shifted to an up-glacier section at approximately ∼2.0–4.0 km along the longitudinal profile.

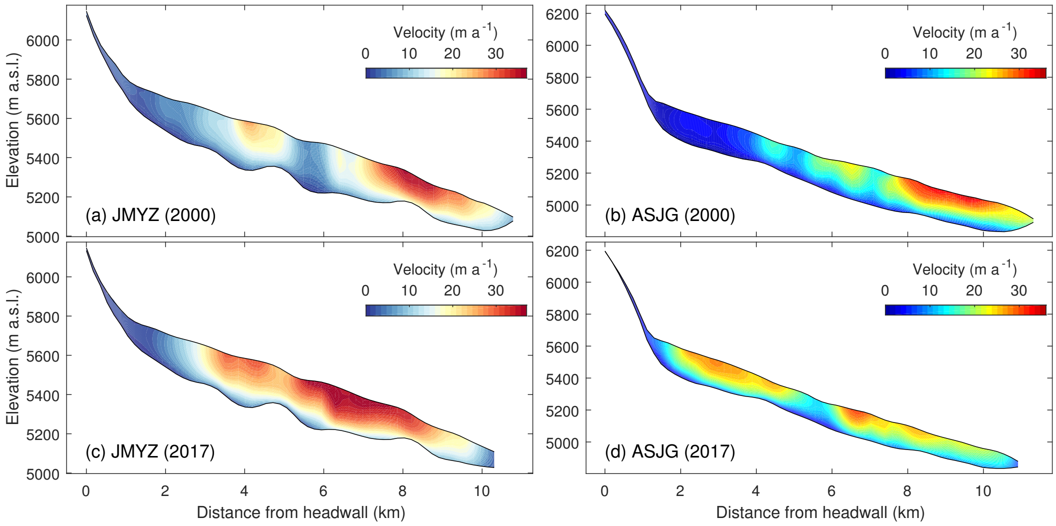

Figure 8. Comparison of temporal variations in flow regimes for lake-terminating glaciers in 2000 and 2017. (**a**,**c**) JMYZ Glacier. (**b**,**d**) ASJG Glacier.

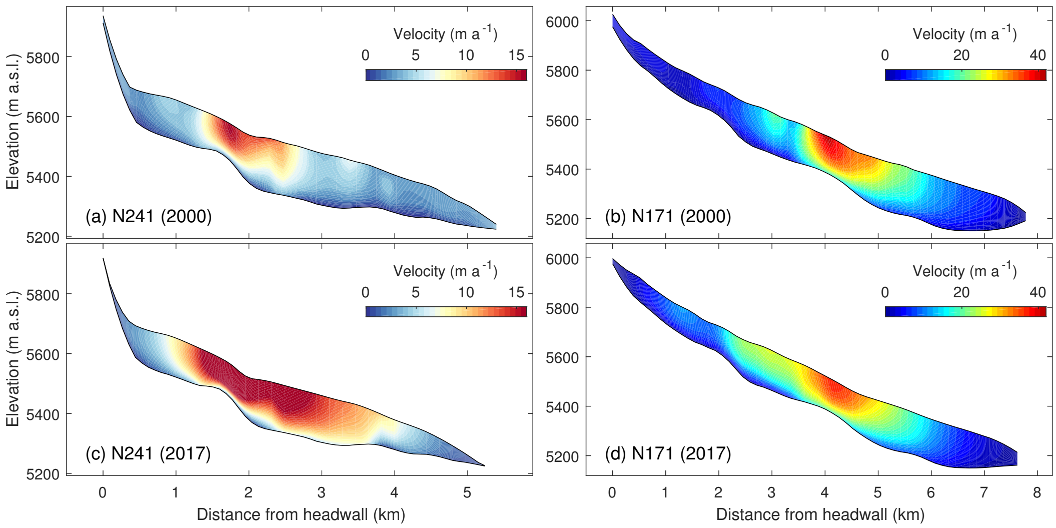

Figure 9. Comparison of temporal variations in flow regimes for land-terminating glaciers in 2000 and 2017. (**a**,**c**) N241 Glacier. (**b**,**d**) N171 Glacier.

For the land-terminating glaciers, i.e., N241 Glacier and N171 Glacier, their flow regime changes can be characterized as accelerating and stable. The velocity fields of N241 showed a substantial transition from a slower to a faster flow pattern during 2000–2017 (Figure 9b,d). In 2000, the high flow zone was located in the central section (∼1.5–2.5 km) of the longitudinal profile. However, by 2017, the high-velocity zone had significantly expanded covering the section ∼1.0–4.0 km along the longitudinal profile, and the basal layer also exhibited fast flow speeds. The N171 Glacier showed a relatively stable flow structure, even though the glacier surface largely thinned during this period (Figure 9a,c).

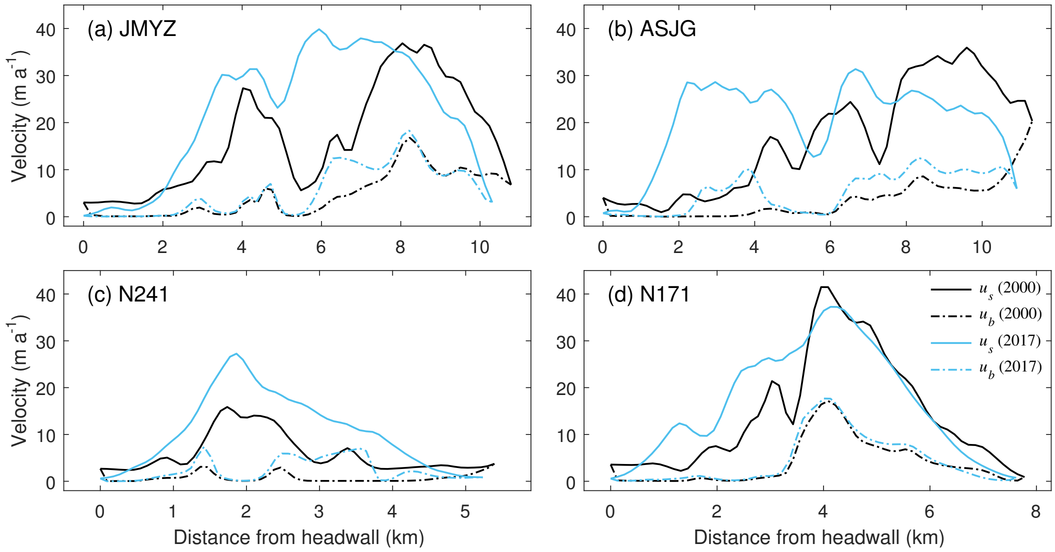

Figure 10. Modeled surface and basal velocities for four glaciers. (**a**) JMYZ Glacier. (**b**) ASJG Glacier. (**c**) N241 Glacier. (**d**) N171 Glacier. Black and blue lines indicate the velocities in 2000 and 2017, respectively. Solid and dot-dashed lines indicate the surface and basal velocities, respectively.

5. Discussion

5.1. Reasons for Heterogeneous Glacier Flow Regime Changes

Our numerical modeling revealed highly heterogeneous patterns of glacier flow regimes within our study region, indicating that glacier dynamic changes were controlled by different factors and complex feedbacks. To elucidate the mechanisms underlying the evolution of flow patterns, we performed a force balance analysis along the longitudinal profile (Figures 11 and 12). For stress equilibrium, the driving stress (τ_d) is balanced by resisting forces, which include basal shear stress (τ_b), longitudinal drag (τ_l), and side drag (τ_w) [65]. It should be noted that the longitudinal stress can be either positive or negative.

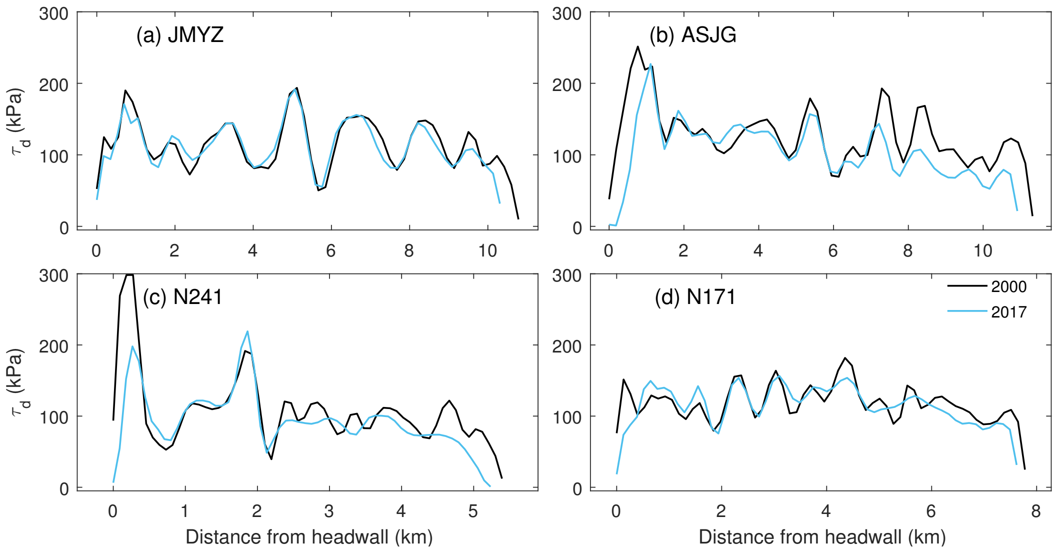

Figure 11. Modeled driving stresses for four glaciers. (**a**) JMYZ Glacier. (**b**) ASJG Glacier. (**c**) N241 Glacier. (**d**) N171 Glacier. Black and blue lines indicate the the results in 2000 and 2017, respectively.

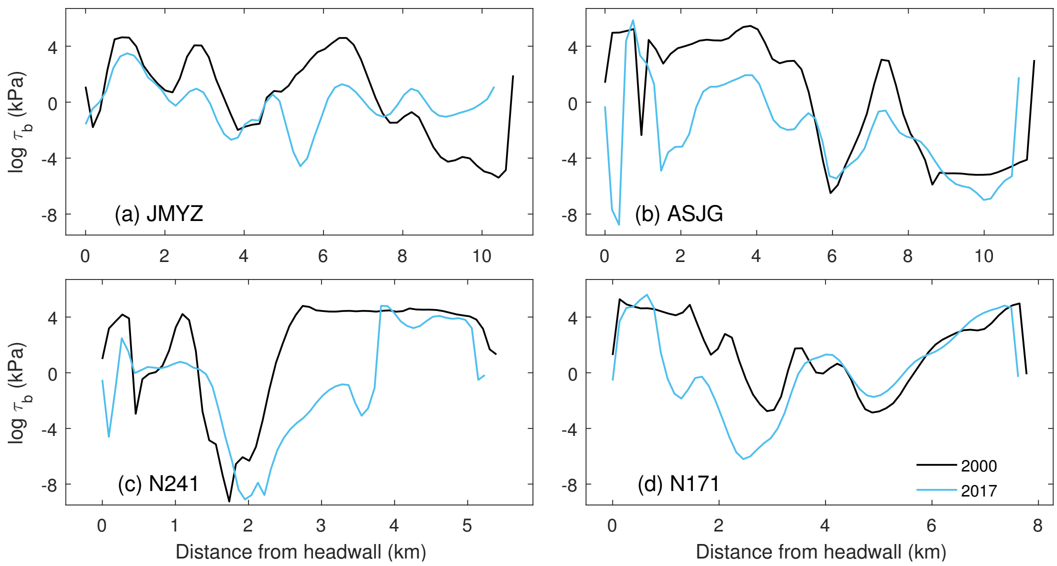

Figure 12. Modeled basal shear stresses for four glaciers. (**a**) JMYZ Glacier. (**b**) ASJG Glacier. (**c**) N241 Glacier. (**d**) N171 Glacier. Black and blue lines indicate the the results in 2000 and 2017, respectively. Note that the y-axis is on a logarithmic scale, representing $\log(\tau_b)$.

The spatial patterns of driving stress (τ_d) on the JMYZ Glacier remained consistent from 2000 to 2017, with only a slight decrease in τ_d observed at the terminus. The slowdown in terminus velocity was due to decreased driving stress and increased basal shear stress, while the accelerated flow in the upper section of the profile can be attributed to a significant reduction in basal shear stress (Figures 8a, 11a and 12a). Longitudinal coupling may have also contributed to the upstream acceleration of ice flow by transmitting the high terminus velocity observed in 2000. Despite the distance between the terminus and the upper fast-flow region being 10 times greater than the average ice thickness of the JMYZ Glacier (approximately 170 m), longitudinal coupling could still influence flow variations upstream from the terminus due to ineffective basal resistance and side drag (Figures S1a and S2a) [65,66].

The driving stress of the ASJG Glacier rapidly decreased between 2000 and 2017, particularly in the lower (7.0–11.0 km) and upper (0.0–2.0 km) sections (Figure 11b), primarily due to reduced ice thickness. This significant reduction in driving stress contributed to the deceleration of terminal velocity (Figures 8b and 10b). The increased flow in the upper section (2.0–4.0 km) was driven by a decrease in basal resistance, which dropped by more than 50% during this period (Figure 12b). While ice-marginal lakes are generally believed to exacerbate mass loss at the terminus, steepen the ice surface, and increase driving stress [28], our findings suggest that sustained mass loss leading to a significant thinning of the ice can largely reduce driving stress and slow down flow speeds.

The fast-flow region of the land-terminating N241 Glacier expanded both upstream and downstream between 2000 and 2017, with significant intensification during this period (Figure 9a,c). Force balance analysis revealed that increased driving stress between approximately $\sim$1.65 and 1.95 km and a substantial decrease in basal shear stress between $\sim$1.9 and 5.0 km were responsible for this expansion and acceleration (Figures 11c and 12c). Additionally, the surface slope of the N241 Glacier steepened around 2.0 km from 2000 to 2017 (Figure 9a,c), further increasing driving stress. Longitudinal coupling played a crucial role in transmitting these increased speeds both upstream and downstream. An extended flow zone became evident in the upper section of the N241 Glacier (Figure S1c). Bedrock topography also played an important role in promoting the downstream acceleration, particularly in areas with steep bedrock gradients. In contrast, the spatio-temporal patterns of the velocity field and force balance terms for the N171 Glacier remained consistent over the study period (Figures 9d–12d, S1d and S2d), indicating relatively stable flow dynamics for this land-terminating glacier. However, there was a slight increase in surface velocities upstream and a decrease downstream around 4.0 km (Figure 10d), which can be attributed to increased basal sliding (Figure 12d).

Our observations and simulations of heterogeneous changes in ice flow regimes within this specific region highlight complexities that may contrast with the widespread reports of glacier slowdown in HMA [67], though our findings are based on a limited sample of four glaciers. The dynamic responses of individual glaciers to climate change are complex and influenced by various factors. However, large-scale satellite studies often emphasize glacier-wide velocity changes without adequately accounting for detailed spatio-temporal variations. This study suggests that the flow dynamics of individual glaciers can be significantly influenced by increased basal sliding due to surface meltwater input and steepened surface slopes. To improve understanding, the future large-scale satellite monitoring of glacier velocity changes should place greater emphasis on capturing the variations among individual glaciers across both space and time.

5.2. Implications for Glacier Evolution Models

Our study reveals that changes in glacier surface velocity are influenced by several factors: surface topography, ice thickness, basal lubrication, subglacial topograph, and longitudinal coupling. These factors, together with external drivers such as climate, affect variations in force balance and consequently the ice flow regime. Current large-scale glacier evolution models can predict future changes in individual glaciers [37,68–70], but they often oversimplify ice dynamics. Some advanced models employ the shallow ice approximation to compute ice flux [68,69], yet they fail to account for longitudinal stress-gradient coupling, subglacial topography, and the impacts of subglacial hydrology on ice dynamics in a changing climate.

In HMA, glacial lakes are projected to increase in number, area, and volume by the end of the century [34]. This expansion will undoubtedly influence glacier mass balance and dynamics. However, current glacier evolution models generally overlook frontal ablation in water-terminating glaciers [71], instead treating glaciers as land-terminating [72]. To improve frontal ablation modeling, glacier evolution models should incorporate ice-lake interactions. Given limited data on marginal lake depth and temperature, developing a parameterization for ice-lake interaction is crucial to reduce computational costs.

Our study also emphasizes that changes in surface topography, particularly in surface slope, can significantly affect driving stress and ice velocity. Accurately modeling changes in surface topography requires a careful consideration of both mass balance and ice dynamics. Many models currently compute elevation-banded surface mass balance [70,71], but this approach introduces uncertainties in spatial surface elevation change. Future models should integrate longitudinal coupling, frontal calving dynamics, and distributed surface mass balance to better capture interactions between ice and marginal lakes, thereby improving projections of ice flow changes. It is essential for next-generation glacier evolution models to incorporate higher-order or full-Stokes dynamics to accurately simulate the complex physical processes responding to climate change [73,74].

5.3. Limitations

In this study, we used multi-sourced datasets, including field measurements, DEMs, satellite optical images, glacier velocity products, and glacier elevation change data, to analyze the changes in land- and lake-terminating glaciers at the headwaters of the YZR. These datasets, however, are not temporally consistent, which created challenges in comparing changes over time in mass balance, terminus position, and velocity. For example, DEMs generated from topographic maps can date back to the 1970s, while other datasets are more reliable only after the 1990s due to the increasing availability of satellite images. Additionally, some of the datasets are open-access global products typically available at relatively coarse spatial resolutions. While these datasets are useful for large-scale analysis, they may lack the spatial detail necessary to capture localized glacier dynamics. The ITS_LIVE velocity product, for instance, provides long-term, high-temporal-resolution data across broad areas, but its 240 m resolution limits the detection of fine-scale velocity variations. To address this limitation, we focused on four relatively large glaciers for detailed analysis.

To characterize and compare the mass and flow changes between land- and lake-terminating glaciers, we selected two of each type from our study region. Ideally, for a meaningful comparison, the selected glaciers would be similar in size (e.g., area, length). However, both lake-terminating glaciers in this region are larger than the land-terminating ones in both area and length. While this selection highlights the dynamic differences between glacier types, some of these differences, particularly in velocity changes, could be influenced by the disparity in glacier size. It is challenging to find glaciers of similar size within the same region that represent both types. A key limitation of this study is the small number of glaciers analyzed, with only two glaciers representing each terminus type. The small sample size and the observed heterogeneity in glacier dynamics limit the generalizability of the findings. Future studies involving more glaciers are necessary to validate and expand these results.

To characterize and compare the mass and flow changes between land- and lake-terminating glaciers, we selected two of each type from our study region based on specific criteria. Both the JMYZ and ASJG Glaciers are definitively identified as lake-terminating and are ideal for studying the impacts of proglacial lakes. To compare these with land-terminating glaciers, we selected the two largest land-terminating glaciers in the region (12.69 km^2 and 17.2 km^2) that are also in close proximity to the lake-terminating glaciers. While this selection enabled us to investigate key dynamic differences, the lake-terminating glaciers are larger (20.7 km^2 and 28.2 km^2), and these size disparities may partially influence velocity changes and other observed differences. Furthermore, the small number of glaciers limits the generalizability of our findings, as high heterogeneity exists not only between different terminus types but also among glaciers of the same type. Despite these limitations, our results provide valuable insights into the spatial and temporal variations in glacier flow regimes, highlighting distinct behaviors between lake- and land-terminating glaciers.

We inferred glacier flow regimes by assuming steady-state geometry and incorporating ITS_LIVE velocity data, using an inversion method to estimate the initial dynamic state of ice flow. However, glacier flow in any given year may not be in equilibrium with its present geometry, as transient effects from past dynamics can still influence current behavior. Our modeling treated the glaciers as isothermal, with a constant flow rate factor, A. In reality, the glaciers in this region are likely polythermal, as ground-penetrating radar detected temperate ice at the basal layer of the JMYZ Glacier [75]. Accurately modeling glacier flow would require thermomechanical modeling that considers transient thermal conditions and surface elevation changes. Despite these limitations, the goal of this study was to capture long-term changes in glacier flow regimes, rather than replicating the precise dynamics of each glacier.

6. Conclusions

This study presents the changes in geometry and flow speed of both land- and lake-terminating glaciers at the YZR headwaters over the past four decades, using a combination of field measurements, remote-sensing observations, and numerical ice flow modeling.

The region-wide average ice mass loss rate more than doubled in the first two decades of the 21st century compared to the period 1974–2000. While lake-terminating glaciers experienced greater mass loss and faster retreat between 1990 and 2019, some land-terminating glaciers exhibited comparable mass loss rates. All glacier terminus types retreated the most during the period 2005–2010.

From 1990 to 2018, larger lake-terminating glaciers consistently exhibited higher flow speeds compared to smaller land-terminating glaciers. Lake-terminating glaciers also displayed more complex and variable velocity trends, whereas land-terminating glaciers typically experienced more uniform acceleration. From 2000 to 2017, lake-terminating glaciers exhibited diverse flow regimes, with some accelerating and others decelerating, while land-terminating glaciers showed either acceleration or stability despite surface thinning.

Our study underscores the significant heterogeneity in glacier behavior in this region, not only between different terminus types but also among glaciers of the same type. For effective water resource and hazard management in the region, it is crucial to monitor the complex dynamics of both glacier types. Improved glacier models are necessary to account for changes in surface topography, longitudinal coupling, and frontal calving dynamics. Incorporating higher-order or full-Stokes dynamics is essential to capture the complex processes driving glacier behavior in a changing climate.

Supplementary Materials: The following supporting information can be downloaded at: https://www.mdpi.com/article/10.3390/rs17010040/s1, Figure S1: Modelled depth-averaged longitudinal drags for four glaciers, (a) JMYZ, (b) ASJG, (c) N241, and (d) N171. Black and blue lines indicate the results in 2000 and 2017, respectively; Figure S2: Modelled depth-averaged side drags for four glaciers, (a) JMYZ, (b) ASJG, (c) N241, and (d) N171. Black and blue lines indicate the the results in 2000 and 2017, respectively.

Author Contributions: Conceptualization, Y.W. (Yuzhe Wang) and M.Z.; methodology, Y.W. (Yuzhe Wang) and M.Z.; writing—review and editing, Y.W. (Yuzhe Wang), M.Z., T.Z., W.S., and Y.W. (Yetang Wang); visualization, Y.W. (Yuzhe Wang) and M.Z. All authors have read and agreed to the published version of the manuscript.

Funding: Yuzhe Wang was supported by the National Natural Science Foundation of China grants 42271134. Weijun Sun was funded by the Taishan Scholars Program of Shandong Province (No. tsqn202312158).

Data Availability Statement: The SRTM data and Landsat images are available through USGS Earth Explorer platform (https://earthexplorer.usgs.gov, accessed on 1 December 2023). TanDEM-X DEM data are available through the Earth Observation Center of the German Aerospace Center (https://geoservice.dlr.de, accessed on 1 December 2023). Glacier outlines are downloaded from http://www.ncdc.ac.cn/portal/metadata/6d44fd19-64d7-4af1-8e81-5fa717585b5b (accessed on 1 December 2023). Glacier thickness data are available from https://doi.org/10.3929/ethz-b-000315707 (accessed on 1 December 2023). ITS_LIVE glacier surface velocities are available from https://nsidc.org/apps/itslive (accessed on 1 December 2023). The SRTM C-X Penetration depth difference data are available from https://data.tpdc.ac.cn/zh-hans/data/24b4dc63-1ae0-45a9-b1ee-eb38f8fd8eb3 (accessed on 1 December 2023). The TOPO DEMs and measured stake velocities can be obtained upon request from the authors.

Acknowledgments: We are grateful to Cunde Xiao and Xiaochen Liu for sharing stake-measured surface velocities on the Jiemayangzong Glacier.

Conflicts of Interest: The authors declare no conflicts of interest.

References

1. Yao, T.; Thompson, L.; Yang, W.; Yu, W.; Gao, Y.; Guo, X.; Yang, X.; Duan, K.; Zhao, H.; Xu, B. Different glacier status with atmospheric circulations in Tibetan Plateau and surroundings. *Nat. Clim. Chang.* **2012**, *2*, 663–667. [CrossRef]
2. Millan, R.; Mouginot, J.; Rabatel, A.; Morlighem, M. Ice velocity and thickness of the world's glaciers. *Nat. Geosci.* **2022**, *15*, 124–129. [CrossRef]
3. Pritchard, H.D. Asia's shrinking glaciers protect large populations from drought stress. *Nature* **2019**, *569*, 649–654. [CrossRef]
4. Lutz, A.F.; Immerzeel, W.W.; Siderius, C.; Wijngaard, R.R.; Nepal, S.; Shrestha, A.B.; Wester, P.; Biemans, H. South Asian agriculture increasingly dependent on meltwater and groundwater. *Nat. Clim. Chang.* **2022**, *12*, 566–573. [CrossRef]
5. Immerzeel, W.W.; Pellicciotti, F.; Bierkens, M.F.P. Rising river flows throughout the twenty-first century in two Himalayan glacierized watersheds. *Nat. Geosci.* **2013**, *6*, 742–745. [CrossRef]
6. Huss, M.; Hock, R. Global-scale hydrological response to future glacier mass loss. *Nat. Clim. Chang.* **2018**, *8*, 135–140. [CrossRef]
7. Nie, Y.; Pritchard, H.D.; Liu, Q.; Hennig, T.; Wang, W.; Wang, X.; Liu, S.; Nepal, S.; Samyn, D.; Hewitt, K.; et al. Glacial change and hydrological implications in the Himalaya and Karakoram. *Nat. Rev. Earth Environ.* **2021**, *2*, 91–106. [CrossRef]
8. Biemans, H.; Siderius, C.; Lutz, A.F.; Nepal, S.; Ahmad, B.; Hassan, T.; von Bloh, W.; Wijngaard, R.R.; Wester, P.; Shrestha, A.B.; et al. Importance of snow and glacier meltwater for agriculture on the Indo-Gangetic Plain. *Nat. Sustain.* **2019**, *2*, 594–601. [CrossRef]
9. Li, D.; Lu, X.; Walling, D.E.; Zhang, T.; Steiner, J.F.; Wasson, R.J.; Harrison, S.; Nepal, S.; Nie, Y.; Immerzeel, W.W.; et al. High Mountain Asia hydropower systems threatened by climate-driven landscape instability. *Nat. Geosci.* **2022**, *15*, 520–530. [CrossRef]
10. Wood, L.R.; Neumann, K.; Nicholson, K.N.; Bird, B.W.; Dowling, C.B.; Sharma, S. Melting Himalayan Glaciers Threaten Domestic Water Resources in the Mount Everest Region, Nepal. *Front. Earth Sci.* **2020**, *8*, 128. [CrossRef]
11. Zhou, Y.; Li, Z.; Li, J.; Zhao, R.; Ding, X. Glacier mass balance in the Qinghai–Tibet Plateau and its surroundings from the mid-1970s to 2000 based on Hexagon KH-9 and SRTM DEMs. *Remote. Sens. Environ.* **2018**, *210*, 96–112. [CrossRef]
12. Bhattacharya, A.; Bolch, T.; Mukherjee, K.; King, O.; Menounos, B.; Kapitsa, V.; Neckel, N.; Yang, W.; Yao, T. High Mountain Asian glacier response to climate revealed by multi-temporal satellite observations since the 1960s. *Nat. Commun.* **2021**, *12*, 4133. [CrossRef]
13. Brun, F.; Berthier, E.; Wagnon, P.; Kääb, A.; Treichler, D. A spatially resolved estimate of High Mountain Asia glacier mass balances from 2000 to 2016. *Nat. Geosci.* **2017**, *10*, 668–673. [CrossRef]
14. Maurer, J.M.; Schaefer, J.M.; Rupper, S.; Corley, A. Acceleration of ice loss across the Himalayas over the past 40 years. *Sci. Adv.* **2019**, *5*, eaav7266. [CrossRef]
15. Shean, D.E.; Bhushan, S.; Montesano, P.; Rounce, D.R.; Arendt, A.; Osmanoglu, B. A Systematic, Regional Assessment of High Mountain Asia Glacier Mass Balance. *Front. Earth Sci.* **2020**, *7*, 363–381. [CrossRef]
16. Veh, G.; Korup, O.; Walz, A. Hazard from Himalayan glacier lake outburst floods. *Proc. Natl. Acad. Sci. USA* **2020**, *117*, 907–912. [CrossRef] [PubMed]
17. Shugar, D.H.; Jacquemart, M.; Shean, D.; Bhushan, S.; Upadhyay, K.; Sattar, A.; Schwanghart, W.; McBride, S.; de Vries, M.V.W.; Mergili, M.; et al. A massive rock and ice avalanche caused the 2021 disaster at Chamoli, Indian Himalaya. *Science* **2021**, *373*, 300–306. [CrossRef]
18. Fujita, K.; Nuimura, T. Spatially heterogeneous wastage of Himalayan glaciers. *Proc. Natl. Acad. Sci. USA* **2011**, *108*, 14011–14014. [CrossRef]
19. Azam, M.F.; Wagnon, P.; Berthier, E.; Vincent, C.; Fujita, K.; Kargel, J.S. Review of the status and mass changes of Himalayan-Karakoram glaciers. *J. Glaciol.* **2018**, *64*, 61–74. [CrossRef]
20. Ragettli, S.; Bolch, T.; Pellicciotti, F. Heterogeneous glacier thinning patterns over the last 40 years in Langtang Himal, Nepal. *Cryosphere* **2016**, *10*, 2075–2097. [CrossRef]
21. King, O.; Quincey, D.J.; Carrivick, J.L.; Rowan, A.V. Spatial variability in mass loss of glaciers in the Everest region, central Himalayas, between 2000 and 2015. *Cryosphere* **2017**, *11*, 407–426. [CrossRef]
22. Zhang, G.; Bolch, T.; Allen, S.; Linsbauer, A.; Chen, W.; Wang, W. Glacial lake evolution and glacier–lake interactions in the Poiqu River basin, central Himalaya, 1964–2017. *J. Glaciol.* **2019**, *65*, 347–365. [CrossRef]
23. King, O.; Bhattacharya, A.; Bhambri, R.; Bolch, T. Glacial lakes exacerbate Himalayan glacier mass loss. *Sci. Rep.* **2019**, *9*, 18145. [CrossRef]
24. Liu, Q.; Mayer, C.; Wang, X.; Nie, Y.; Wu, K.; Wei, J.; Liu, S. Interannual flow dynamics driven by frontal retreat of a lake-terminating glacier in the Chinese Central Himalaya. *Earth Planet. Sci. Lett.* **2020**, *546*, 116450. [CrossRef]
25. Wei, J.; Liu, S.; Wang, X.; Zhang, Y.; Jiang, Z.; Wu, K.; Zhang, Z.; Zhang, T. Longbasaba Glacier recession and contribution to its proglacial lake volume between 1988 and 2018. *J. Glaciol.* **2021**, *67*, 473–484. [CrossRef]
26. Zhang, G.; Bolch, T.; Yao, T.; Rounce, D.R.; Chen, W.; Veh, G.; King, O.; Allen, S.K.; Wang, M.; Wang, W. Underestimated mass loss from lake-terminating glaciers in the greater Himalaya. *Nat. Geosci.* **2023**, *16*, 333–338. [CrossRef]
27. Benn, D.I.; Warren, C.R.; Mottram, R.H. Calving processes and the dynamics of calving glaciers. *Earth-Sci. Rev.* **2007**, *82*, 143–179. [CrossRef]
28. Carrivick, J.L.; Tweed, F.S. Proglacial lakes: Character, behaviour and geological importance. *Quat. Sci. Rev.* **2013**, *78*, 34–52. [CrossRef]
29. King, O.; Dehecq, A.; Quincey, D.; Carrivick, J. Contrasting geometric and dynamic evolution of lake and land-terminating glaciers in the central Himalaya. *Glob. Planet. Chang.* **2018**, *167*, 46–60. [CrossRef]

30. Tsutaki, S.; Fujita, K.; Nuimura, T.; Sakai, A.; Sugiyama, S.; Komori, J.; Tshering, P. Contrasting thinning patterns between lake- and land-terminating glaciers in the Bhutanese Himalaya. *Cryosphere* **2019**, *13*, 2733–2750. [CrossRef]
31. Pronk, J.B.; Bolch, T.; King, O.; Wouters, B.; Benn, D.I. Contrasting surface velocities between lake- and land-terminating glaciers in the Himalayan region. *Cryosphere* **2021**, *15*, 5577–5599. [CrossRef]
32. Carrivick, J.L.; Tweed, F.S.; Sutherland, J.L.; Mallalieu, J. Toward Numerical Modeling of Interactions Between Ice-Marginal Proglacial Lakes and Glaciers. *Front. Earth Sci.* **2020**, *8*, 577068. [CrossRef]
33. Scoffield, A.C.; Rowan, A.V.; Quincey, D.J.; Carrivick, J.L.; Sole, A.J.; Cook, S.J. Sub-regional variability in the influence of ice-contact lakes on Himalayan glaciers. *J. Glaciol.* **2024**, 1–11. [CrossRef]
34. Furian, W.; Maussion, F.; Schneider, C. Projected 21st-Century Glacial Lake Evolution in High Mountain Asia. *Front. Earth Sci.* **2022**, *10*, 821798. [CrossRef]
35. Azam, M.F. Need of integrated monitoring on reference glacier catchments for future water security in Himalaya. *Water Secur.* **2021**, *14*, 100098. [CrossRef]
36. Hock, R.; Bliss, a.; Marzeion, B.; Giesen, R.H.; Hirabayashi, Y.; Huss, M.; Radić, V.; Slangen, A.B.A. GlacierMIP—A model intercomparison of global-scale glacier mass-balance models and projections. *J. Glaciol.* **2019**, *65*, 453–467. [CrossRef]
37. Marzeion, B.; Hock, R.; Anderson, B.; Bliss, A.; Champollion, N.; Fujita, K.; Huss, M.; Immerzeel, W.W.; Kraaijenbrink, P.; Malles, J.H.; et al. Partitioning the Uncertainty of Ensemble Projections of Global Glacier Mass Change. *Earth's Future* **2020**, *8*, e2019EF001470. [CrossRef]
38. Zekollari, H.; Huss, M.; Farinotti, D.; Lhermitte, S. Ice-Dynamical Glacier Evolution Modeling—A Review. *Rev. Geophys.* **2022**, *60*, e2021RG000754. [CrossRef]
39. Guo, W.; Liu, S.; Xu, J.; Wu, L.; Shangguan, D.; Yao, X.; Wei, J.; Bao, W.; Yu, P.; Liu, Q.; et al. The second Chinese glacier inventory: Data, methods and results. *J. Glaciol.* **2015**, *61*, 357–372. [CrossRef]
40. Wang, X.; Guo, X.; Yang, C.; Liu, Q.; Wei, J.; Zhang, Y.; Liu, S.; Zhang, Y.; Jiang, Z.; Tang, Z. Glacial lake inventory of high-mountain Asia in 1990 and 2018 derived from Landsat images. *Earth Syst. Sci. Data* **2020**, *12*, 2169–2182. [CrossRef]
41. Ma, X.; Xiao, G.; Duan, Y. *Compilation Specifications for National Fundamental Scale Maps. Part 1: Compliation Specifications for 1:25,000 1:50,000 1:100,000 Topographic Maps*; Technical Report; State Bureau of Surveying and Mapping: Beijing, China, 2008.
42. Kääb, A.; Treichler, D.; Nuth, C.; Berthier, E. Brief Communication: Contending estimates of 2003–2008 glacier mass balance over the Pamir-Karakoram-Himalaya. *Cryosphere* **2015**, *9*, 557–564. [CrossRef]
43. Braun, M.H.; Malz, P.; Sommer, C.; Farías-Barahona, D.; Sauter, T.; Casassa, G.; Soruco, A.; Skvarca, P.; Seehaus, T.C. Constraining glacier elevation and mass changes in South America. *Nat. Clim. Chang.* **2019**, *9*, 130–136. [CrossRef]
44. Zhou, Y.; Li, X.; Zheng, D.; Li, Z. Evolution of geodetic mass balance over the largest lake-terminating glacier in the Tibetan Plateau with a revised radar penetration depth based on multi-source high-resolution satellite data. *Remote Sens. Environ.* **2022**, *275*, 113029. [CrossRef]
45. Gdulová, K.; Marešová, J.; Moudrý, V. Accuracy assessment of the global TanDEM-X digital elevation model in a mountain environment. *Remote Sens. Environ.* **2020**, *241*, 111724. [CrossRef]
46. Hugonnet, R.; McNabb, R.; Berthier, E.; Menounos, B.; Nuth, C.; Girod, L.; Farinotti, D.; Huss, M.; Dussaillant, I.; Brun, F.; et al. Accelerated global glacier mass loss in the early twenty-first century. *Nature* **2021**, *592*, 726–731. [CrossRef] [PubMed]
47. Nuth, C.; Kääb, A. Co-registration and bias corrections of satellite elevation data sets for quantifying glacier thickness change. *Cryosphere* **2011**, *5*, 271–290. [CrossRef]
48. Gardelle, J.; Berthier, E.; Arnaud, Y. Impact of resolution and radar penetration on glacier elevation changes computed from DEM differencing. *J. Glaciol.* **2012**, *58*, 419–422. [CrossRef]
49. Li, C.; Jiang, L.; Liu, L.; Wang, H. Regional and Altitude-Dependent Estimate of the SRTM C/X-Band Radar Penetration Difference on High Mountain Asia Glaciers. *IEEE J. Sel. Top. Appl. Earth Obs. Remote Sens.* **2021**, *14*, 4244–4253. [CrossRef]
50. Holzer, N.; Vijay, S.; Yao, T.; Xu, B.; Buchroithner, M.; Bolch, T. Four decades of glacier variations at Muztagh Ata (eastern Pamir): A multi-sensor study including Hexagon KH-9 and Pléiades data. *Cryosphere* **2015**, *9*, 2071–2088. [CrossRef]
51. Huss, M. Density assumptions for converting geodetic glacier volume change to mass change. *Cryosphere* **2013**, *7*, 877–887. [CrossRef]
52. Mannerfelt, E.S.; Dehecq, A.; Hugonnet, R.; Hodel, E.; Huss, M.; Bauder, A.; Farinotti, D. Halving of Swiss glacier volume since 1931 observed from terrestrial image photogrammetry. *Cryosphere* **2022**, *16*, 3249–3268. [CrossRef]
53. Pfeffer, W.T.; Arendt, A.A.; Bliss, A.; Bolch, T.; Cogley, J.G.; Gardner, A.S.; Hagen, J.O.; Hock, R.; Kaser, G.; Kienholz, C.; et al. The Randolph Glacier Inventory: A globally complete inventory of glaciers. *J. Glaciol.* **2014**, *60*, 537–552. [CrossRef]
54. Gardner, A.; Fahnestock, M.; Scambos, T. MEASURES ITS_LIVE Regional Glacier and Ice Sheet Surface Velocities. 2019. Available online: https://nsidc.org/data/nsidc-0776/versions/1 (accessed on 1 December 2023).
55. King, O.; Bhattacharya, A.; Bolch, T. The presence and influence of glacier surging around the Geladandong ice caps, North East Tibetan Plateau. *Adv. Clim. Chang. Res.* **2021**, *12*, 299–312. [CrossRef]
56. Downs, J.; Johnson, J.V. A rapidly retreating, marine-terminating glacier's modeled response to perturbations in basal traction. *J. Glaciol.* **2022**, *68*, 891–900. [CrossRef]

57. Yellala, A.; Kumar, V.; Høgda, K.A. Bara Shigri and Chhota Shigri glacier velocity estimation in western Himalaya using Sentinel-1 SAR data. *Int. J. Remote Sens.* **2019**, *40*, 5861–5874. [CrossRef]
58. Zhang, Z.; Xu, Y.; Liu, S.; Ding, J.; Zhao, J. Seasonal variations in glacier velocity in the High Mountain Asia region during 2015–2020. *J. Arid Land* **2023**, *15*, 637–648. [CrossRef]
59. Farinotti, D.; Huss, M.; Fürst, J.J.; Landmann, J.; Machguth, H.; Maussion, F.; Pandit, A. A consensus estimate for the ice thickness distribution of all glaciers on Earth. *Nat. Geosci.* **2019**, *12*, 168–173. [CrossRef]
60. Wang, Y.; Zhang, T.; Xiao, C.; Ren, J.; Wang, Y. A two-dimensional, higher-order, enthalpy-based thermomechanical ice flow model for mountain glaciers and its benchmark experiments. *Comput. Geosci.* **2020**, *141*, 104526. [CrossRef]
61. Yan, Z.; Zhang, T.; Wang, Y.; Leng, W.; Ding, M.; Zhang, D.; Xiao, C. Dynamic Evolution Modeling of a Lake-Terminating Glacier in the Western Himalayas Using a Two-Dimensional Higher-Order Flowline Model. *Remote Sens.* **2022**, *14*, 6189. [CrossRef]
62. Arthern, R.J.; Gudmundsson, G.H. Initialization of ice-sheet forecasts viewed as an inverse Robin problem. *J. Glaciol.* **2010**, *56*, 527–533. [CrossRef]
63. Schäfer, M.; Zwinger, T.; Christoffersen, P.; Gillet-Chaulet, F.; Laakso, K.; Pettersson, R.; Pohjola, V.A.; Strozzi, T.; Moore, J.C. Sensitivity of basal conditions in an inverse model: Vestfonna ice cap, Nordaustlandet/Svalbard. *Cryosphere* **2012**, *6*, 771–783. [CrossRef]
64. Jay-Allemand, M.; Gillet-Chaulet, F.; Gagliardini, O.; Nodet, M. Investigating changes in basal conditions of Variegated Glacier prior to and during its 1982-1983 surge. *Cryosphere* **2011**, *5*, 659–672. [CrossRef]
65. Cuffey, K.; Paterson, W. *The Physics of Glaciers*, 4th ed.; Elsevier: Amsterdam, The Netherlands, 2010. [CrossRef]
66. Price, S.; Payne, A.; Catania, G.; Neumann, T. Seasonal acceleration of inland ice via longitudinal coupling to marginal ice. *J. Glaciol.* **2008**, *54*, 213–219. [CrossRef]
67. Dehecq, A.; Gourmelen, N.; Gardner, A.S.; Brun, F.; Goldberg, D.; Nienow, P.W.; Berthier, E.; Vincent, C.; Wagnon, P.; Trouvé, E. Twenty-first century glacier slowdown driven by mass loss in High Mountain Asia. *Nat. Geosci.* **2019**, *12*, 22–27. [CrossRef]
68. Maussion, F.; Butenko, A.; Champollion, N.; Dusch, M.; Eis, J.; Fourteau, K.; Gregor, P.; Jarosch, A.H.; Landmann, J.; Oesterle, F.; et al. The Open Global Glacier Model (OGGM) v1.1. *Geosci. Model Dev.* **2019**, *12*, 909–931. [CrossRef]
69. Zekollari, H.; Huss, M.; Farinotti, D. Modelling the future evolution of glaciers in the European Alps under the EURO-CORDEX RCM ensemble. *Cryosphere* **2019**, *13*, 1125–1146. [CrossRef]
70. Rounce, D.R.; Hock, R.; Shean, D.E. Glacier Mass Change in High Mountain Asia Through 2100 Using the Open-Source Python Glacier Evolution Model (PyGEM). *Front. Earth Sci.* **2020**, *7*, 331. [CrossRef]
71. Huss, M.; Hock, R. A new model for global glacier change and sea-level rise. *Front. Earth Sci.* **2015**, *3*, 54–75. [CrossRef]
72. Rounce, D.R.; Hock, R.; Maussion, F.; Hugonnet, R.; Kochtitzky, W.; Huss, M.; Berthier, E.; Brinkerhoff, D.; Compagno, L.; Copland, L.; et al. Global glacier change in the 21st century: Every increase in temperature matters. *Science* **2023**, *379*, 78–83. [CrossRef]
73. Van Tricht, L.; Huybrechts, P. Modelling the historical and future evolution of six ice masses in the Tien Shan, Central Asia, using a 3D ice-flow model. *Cryosphere* **2023**, *17*, 4463–4485. [CrossRef]
74. Wijngaard, R.R.; Herrington, A.R.; Lipscomb, W.H.; Leguy, G.R.; An, S.I. Exploring the ability of the variable-resolution Community Earth System Model to simulate cryospheric–hydrological variables in High Mountain Asia. *Cryosphere* **2023**, *17*, 3803–3828. [CrossRef]
75. Zhang, T.; Ding, M.; Xiao, C.; Zhang, D.; Du, Z. Temperate ice layer found in the upper area of Jima Yangzong Glacier, the headstream of Yarlung Zangbo River. *Sci. Bull.* **2016**, *61*, 619–621. [CrossRef]